The Astrophysical Journal, 1002:83 (11pp), 2026 May 1 https://doi.org/10.3847/1538-4357/ae595d

© 2026. The Author(s). Published by the American Astronomical Society.
OPEN ACCESS

Discovery of a Likely Type II Supernova at $z = 3.6$ with JWST

D. A. Coulter[1], J. D. R. Pierel[1,20], C. DeCoursey[2], T. J. Moriya[3,4,5], M. R. Siebert[1], B. A. Joshi[6], M. Engesser[1], A. Rest[1,6], E. Egami[2], M. Shahbandeh[1], W. Chen[7], O. D. Fox[1], L. G. Strolger[1], Y. Zenati[1,6,21], A. J. Bunker[8], P. A. Cargile[9], M. Curti[10], D. J. Eisenstein[9], S. Gezari[1,6], S. Gomez[9], M. Guolo[6], K. Hainline[2], J. Jencson[11], B. D. Johnson[9], M. Karmen[6], R. Maiolino[12,13,14], R. M. Quimby[15,16], P. Rinaldi[2], B. Robertson[17], S. Tacchella[12,13], F. Sun[9], Q. Wang[18], and T. Wevers[1,19]

[1] Space Telescope Science Institute, Baltimore, MD 21218, USA; dcoulter@stsci.edu
[2] Steward Observatory, University of Arizona, 933 North Cherry Avenue, Tucson, AZ 85721, USA
[3] National Astronomical Observatory of Japan, National Institutes of Natural Sciences, 2-21-1 Osawa, Mitaka, Tokyo 181-8588, Japan
[4] Graduate Institute for Advanced Studies, SOKENDAI, 2-21-1 Osawa, Mitaka, Tokyo 181-8588, Japan
[5] School of Physics and Astronomy, Monash University, Clayton, VIC 3800, Australia
[6] Physics and Astronomy Department, Johns Hopkins University, Baltimore, MD 21218, USA
[7] Department of Physics, Oklahoma State University, 145 Physical Sciences Building, Stillwater, OK 74078, USA
[8] Department of Physics, University of Oxford, Denys Wilkinson Building, Keble Road, Oxford OX1 3RH, UK
[9] Center for Astrophysics | Harvard & Smithsonian, 60 Garden Street, Cambridge, MA 02138, USA
[10] European Southern Observatory, Karl-Schwarzschild-Strasse 2, 85748 Garching, Germany
[11] IPAC, Mail Code 100-22, California Institute of Technology, 1200 East California Boulevard, Pasadena, CA 91125, USA
[12] Kavli Institute for Cosmology, University of Cambridge, Madingley Road, Cambridge CB3 0HA, UK
[13] Cavendish Laboratory, University of Cambridge, 19 JJ Thomson Avenue, Cambridge CB3 0HE, UK
[14] Department of Physics and Astronomy, University College London, Gower Street, London WC1E 6BT, UK
[15] Department of Astronomy/Mount Laguna Observatory, San Diego State University, 5500 Campanile Drive, San Diego, CA 92812-1221, USA
[16] Kavli Institute for the Physics and Mathematics of the Universe (WPI), The University of Tokyo Institutes for Advanced Study, The University of Tokyo, Kashiwa, Chiba 277-8583, Japan
[17] Department of Astronomy and Astrophysics, University of California, Santa Cruz, 1156 High Street, Santa Cruz, CA 96054, USA
[18] Department of Physics and Kavli Institute for Astrophysics and Space Research, Massachusetts Institute of Technology, 77 Massachusetts Avenue, Cambridge, MA 02139, USA
[19] Astrophysics & Space Institute, Schmidt Sciences, New York, NY 10011, USA

Received 2025 January 22; revised 2026 March 26; accepted 2026 March 26; published 2026 April 28

Abstract

Transient astronomy of the early, high-redshift ($z > 3$) Universe is an unexplored regime that offers the possibility of probing the first stars and the epoch of reionization. During Cycles 1 and 2 of the James Webb Space Telescope (JWST), the JWST Advanced Deep Extragalactic Survey program enabled one of the first searches for transients in deep images (∼30 AB mag) over a relatively wide area (25 arcmin^2). One transient, AT 2023adsv, was discovered with an F200W magnitude of 28.04 AB mag, and subsequent JWST observations revealed that the transient is a likely supernova (SN) in a host with $z_{\rm spec} = 3.613 \pm 0.001$ and an inferred metallicity at the position of the SN of $Z_* = 0.3 \pm 0.1\ Z_\odot$. At this redshift, the first detections in F115W and F150W show that AT 2023adsv had bright rest-frame UV flux at the time of discovery. The multiband light curve of AT 2023adsv is best matched by a template of a Type IIP SN (SN IIP) with a peak absolute magnitude of $M_B \approx -18.3$ AB mag. We find a good match to a 20 $M_\odot$ red supergiant progenitor star with an explosion energy of 2×10^{51} erg, likely higher than normally observed in the local Universe, but consistent with SNe IIP drawn from local, lower-metallicity environments. AT 2023adsv is the most distant photometrically classified SN IIP yet discovered with a spectroscopic redshift measurement, and may represent a global shift in SN IIP properties as a function of redshift.

Unified Astronomy Thesaurus concepts: Supernovae (1668); Core-collapse supernovae (304); Type II supernovae (1731); High-redshift galaxies (734); Metallicity (1031)

1. Introduction

Core-collapse supernovae (CCSNe) are the explosive deaths of massive stars with initial masses $> 8\ M_\odot$ and are remarkably diverse in their properties (A. Heger et al. 2003; S. J. Smartt 2009; J. P. Anderson et al. 2014; N. E. Sanders et al. 2015; S. Valenti et al. 2016; C. P. Gutiérrez et al. 2017). This diversity is driven by the broad range of their progenitor masses, binarity, mass-loss history, rotation, and metallicity, which sensitively affect their evolution, setting the initial conditions for both their stellar structure and circumstellar environments prior to collapse and resulting in a similarly broad range of explosion energies, ejecta compositions, and observed luminosities (A. Gal-Yam et al. 2014; N. Smith 2014; S. Wu & J. Fuller 2021). These explosions connect to astrophysical phenomena across many scales—due to their high mass, the progenitors of CCSNe produce ionizing photons that contribute to the reionization of the Universe. Their short lifetimes allow these explosions to trace both the instantaneous star formation rate (SFR) of their locales, and their rate constrain the high-mass end of the initial mass

---

[20] NASA Einstein Fellow.
[21] ISEF International Fellowship.

Original content from this work may be used under the terms of the Creative Commons Attribution 4.0 licence. Any further distribution of this work must maintain attribution to the author(s) and the title of the work, journal citation and DOI.

function (IMF). Consequently, these supernovae (SNe) profoundly affect their explosion sites through the energy, momentum, and nucleosynthetic yields that they deposit into into the interstellar medium, providing a feedback mechanism to moderate star formation and acting as factories for cosmic dust (N. Lahén et al. 2024).

This diversity yields a wide range of luminosities, and in particular for CCSNe—across all subtypes—their peak B-band magnitudes range from $-16.8 > \bar{M}_B > -18.6$ mag, making them luminous enough to be observed at cosmological distances (D. Richardson et al. 2014). Moreover, while Type Ia SNe (SNe Ia) are in general more luminous (~ -19 mag), because their progenitors arise from lower-mass stars, the delay time between their formation and explosion is much longer than that of CCSNe. Therefore, we expect to detect fewer SNe Ia at high redshift (L.-G. Strolger et al. 2010, 2020; S. A. Rodney et al. 2014), making luminous CCSNe intriguing probes of the early Universe.

In the last two decades, work based on the Hubble Space Telescope (HST) has pushed the study of CCSNe rates and properties to further distances (M. T. Botticella et al. 2008; G. Bazin et al. 2009; O. Graur et al. 2011; T. Dahlen et al. 2012; J. Melinder et al. 2012), culminating with observations from the Cosmic Assembly Near-infrared Deep Extragalactic Legacy Survey (N. A. Grogin et al. 2011; A. M. Koekemoer et al. 2011) and Cluster Lensing and Supernova survey with HST (M. Postman et al. 2012), which constrained the CCSN rate out to $z \approx 2.5$ (L.-G. Strolger et al. 2015).

The optical emission for CCSNe discovered at even greater distances ($z > 2.5$) will peak at wavelengths of 2 μm and beyond, placing more distant samples out of reach for HST but not for the James Webb Space Telescope (JWST). Indeed, JWST is already removing this barrier to discovering distant and observer-frame IR bright CCSNe due to its combination of wavelength coverage and sensitivity, opening a new frontier in transient astronomy with the discovery of several high-z SNe since its launch (W. Chen et al. 2022; M. Engesser et al. 2022a, 2022b; C. DeCoursey et al. 2023a, 2023b; J. D. R. Pierel et al. 2025, 2024a, 2024b, 2024c; M. R. Siebert et al. 2024). Such discoveries are vital laboratories to test whether SN properties, including their rates and explosion characteristics, are affected by global environmental changes like metallicity across cosmic time.

Indeed, lower metallicities can reduce a progenitor's mass-loss rate due to the suppression of stellar winds (J. S. Vink et al. 2001; M. R. Mokiem et al. 2007), and if the star is initially rotating, can limit the amount of angular momentum lost, resulting in deeper mixing. This rotationally induced mixing can in turn lead to larger helium cores prior to collapse, and produce more energetic explosions (S. E. Woosley et al. 2002). In general, if environmental conditions systematically result in the alteration of the internal structure of massive stars with respect to their local counterparts, we may expect a corresponding evolution in observed Type II SN (SN II) properties, such as their resulting colors, peak luminosities, and for Type IIP SNe (SNe IIP), their plateau durations (D. V. Popov 1993; A. Heger et al. 2003; L. Dessart et al. 2013). In addition to testing whether and how SN properties change as a function of redshift, important questions such as whether the CCSN rate follows the cosmic SFR density or if the high-mass end of the IMF flattens with redshift in low-metallicity stellar populations (R. B. Larson 1998; J. J. Ziegler et al. 2022) is only possible by building a sample of high-z CCSNe.

Recent studies of nearby SNe II have suggested a link between the metallicity of the host galaxy and an SN II's spectral and photometric properties (J. P. Anderson et al. 2016; F. Taddia et al. 2016; C. P. Gutiérrez et al. 2017, 2018), and theoretical work has suggested that SNe IIP may be effective probes of a host's underlying metallicity if properly calibrated (L. Dessart et al. 2014). This prediction was tested by an empirical study of 12 SNe II in low-luminosity host galaxies (i.e., low metallicity via the mass–metallicity relationship (MZR)), which showed that these SNe tend to be up to $\sim$0.5 mag more luminous than the average SN II at solar metallicities. In agreement with the prediction from L. Dessart et al. (2014), it was also observed that the depth of the pseudo-equivalent width (pEW) of Fe II (λ5018) was suppressed at lower metallicity (S. Scott et al. 2019, hereafter S19).

These findings are potentially biased, however, by the fact that most SNe II have been discovered within the local Universe where hosts tend to be luminous and at solar metallicity. Local, notable exceptions include the discovery of SN 20015bs, which purports that its progenitor was particularly massive with a zero age main-sequence (ZAMS) mass of $\approx$17–25 $M_\odot$ (J. P. Anderson et al. 2018), and SN 2023ufx, a luminous ($M_g \approx -18.5$ mag) SN II discovered in a low-metallicity dwarf galaxy (M. A. Tucker et al. 2024); both SNe have metallicities of $Z \leqslant 0.1\, Z_\odot$, and both are potential analogs to SNe II discovered at high z. However, these assertions need to be tested through the discovery of many more CCSNe in the early Universe.

Fortunately, this is a task to which JWST is particularly well suited. The JWST Advanced Deep Extragalactic Survey (JADES) program (D. J. Eisenstein et al. 2025) observed $\sim$25 arcmin^2 of the sky to depths of $m_{\mathrm{AB}} \gtrapprox 30$ in nine NIRCam filters in two separate epochs, the first between 2022 September 29 and October 5, and the second between 2023 September 28 and October 3. These repeated observations allowed for these images to be subtracted to discover new transients beyond the redshift limitations of HST, with a sensitivity for CCSNe to $z > 4$. Using this $\sim$1 yr baseline dozens of new transient objects were discovered (C. DeCoursey et al. 2025, hereafter D25), and here we present a candidate for one of the most distant SN II discovered to date: AT 2023adsv, a very blue and likely subsolar metallicity SN IIP–like transient located at R.A. $= 3^{\mathrm{h}}32^{\mathrm{m}}39\overset{\mathrm{s}}{.}4574$ and decl. $= -27^{\mathrm{d}}50^{\mathrm{m}}19\overset{\mathrm{s}}{.}6660$ (although see J. Cooke et al. 2012; S. Gomez et al. 2024 for previous high-z superluminous SN candidates). AT 2023adsv is embedded in its host, JADES-GS+53.16439-27.83877, with a spectroscopically confirmed redshift of $z_{\mathrm{spec}} = 3.613 \pm 0.001$.

In what follows, we describe the identification and analysis of AT 2023adsv, as well as a brief comparison to other SNe IIP in the local Universe. This paper is structured as follows. In Section 2, we present a summary of the observations for this SN, our reduction of the data, and obtaining AT 2023adsv's host redshift. In Section 3 we describe our classification of AT 2023adsv as a likely SN II, present the properties of its host, and model AT 2023adsv's light curve. In Section 4 we discuss AT 2023adsv in the context of a sample of local SNe IIP, and in Section 5 we conclude with a discussion on the prospects for building an SN IIP sample at high redshift and its use as a metallicity probe of the Universe, as well as the implications of the new frontier enabled by JWST. Throughout this paper, we assume a standard ΛCDM cosmology with $H_0 = 70\,\mathrm{km\,s^{-1}\,Mpc^{-1}}$ and $\Omega_m = 0.315$.

2. Summary of Observations

AT 2023adsv was discovered as a part of a transient search for the JADES program (D. J. Eisenstein et al. 2026), centered on the Great Observatories Origins Deep Survey's south (GOODS-S) field (M. Giavalisco et al. 2004). A full description of JADES, including its survey design, data products, the selection process for discovering new transients, and the follow-up observations of those subsequent discoveries through its approved Director's Discretionary Time (DDT) program, are described and presented in detail in D25.

To summarize, the first JADES observations were acquired between 2022 September 29 and 2022 October 5, in the NIRCam filters F090W, F115W, F150W, F200W, F277W, F335M, F356W, F410M, and F444W to a 5σ depth of $m_{\mathrm{AB}} \sim 30$. Nearly a year later, a second set of observations in the same filters and to the same depths were taken between 2023 September 29 and 2023 October 3, resulting in an overlapping footprint of ∼25 arcmin^2 (both observations under PID 1180). During this second epoch, several observations failed, and subsets of the field were observed on 2023 November 15 and 2024 January 1. Upon the identification of many interesting transients in color, redshift, and luminosity space (see D25 for a complete accounting), a JWST DDT program was approved to follow-up the most interesting transients in this field (E. Egami et al. 2023). These subsequent observations were obtained on 2023 November 28 (NIRCam filters F115W, F150W, F200W, F277W, F356W, and F444W) and on 2024 January 1 (NIRCam filters F150W, F200W, F277W, F356W, and F444W; PID 6541) with the latter epoch including NIRSpec multiobject spectroscopy (MOS) coverage using the microshutter assembly (MSA; P. Ferruit et al. 2022). NIRSpec covered the most promising ∼10 transients (as well as a variety of galaxy spectra) using the MSA with the prism ($R \sim 100$) grating, of which AT 2023adsv was one of three objects that are described in a pair of companion papers (J. D. R. Pierel et al. 2024a; M. R. Siebert et al. 2024). Below, we describe the data reduction and photometric measurements we derive for AT 2023adsv.

2.1. Measuring Photometry

AT 2023adsv is embedded in a relatively compact host and therefore obtaining accurate photometric measurements requires removing the underlying host light from the SN position. We achieve this through the process of "difference imaging," or subtracting a template image (preferably with no SN light in it) from a series of science images containing the SN flux we wish to measure. For every science epoch, we align each of the underlying JWST Level 2 ("CAL") images to a catalog of JADES galaxies (that has in turn been aligned to Gaia sources), using the JWST/HST Alignment Tool (`JHAT`; A. Rest et al. 2023).[22] CAL images are those that have been bias subtracted, dark subtracted, and flat-fielded but not yet corrected for geometric distortion. We drizzle these CAL files into Level 3 ("I2D") files using the JWST pipeline (H. Bushouse et al. 2022). The extra `JHAT` step improves the relative alignment by an order of magnitude between the epochs (from ∼1 to ∼0.1 pixel), allowing for subtractions with fewer artifacts between the template and science images. To perform the subtraction, we use the High Order Transform of PSF and Template Subtraction (`HOTPANTS`; A. Becker 2015)[23] code (with additional improvements implemented in `photpipe`; A. Rest et al. 2005), resulting in the difference images upon which we perform our photometry (see Figure 1; the right three columns are the difference images [per filter] generated from subtracting the "template" [top, leftmost epoch] from the "science" image [bottom, leftmost image]).

We measure the photometry in the difference images with a process described in J. D. R. Pierel et al. (2025, 2024c), using the `space_phot`[24] Level 3 point-spread function (PSF) fitting routine centered on a 5 × 5 pixel cutout at AT 2023adsv's position. `space_phot` models the Level 3 PSF by drizzling the Level 2 PSF models from `webbpsf`,[25] which account for the spatial and temporal dependence of the JWST PSF and corrects for the losses in flux incurred by imposing a finite aperture. The resulting fluxes, measured in units of MJy sr^{-1}, are converted to AB magnitudes using the native pixel scale of each image ($0\overset{''}{.}03$ pixel^{-1} for short-wavelength images and $0\overset{''}{.}06$ pixel^{-1} for long-wavelength images), and the final, measured photometry is given in Table 1.

2.2. NIRSpec Reduction

We obtained the Stage 2 spectroscopic data collected from the DDT program from the Mikulski Archive for Space Telescopes (see Table 2). With the context file `jwst_1185.pmap`, we used the JWST pipeline (H. Bushouse et al. 2022) to generate the 2D spectrum and applied a correction for slit losses based on the position of the SN within the MSA shutters (Figures 2(a) and (b)). Next, we performed an optimal point-source extraction using the algorithm from K. Horne (1986; implemented as a Jupyter notebook as part of the NIRSpec integral-field unit optimal point-source extraction guide)[26] to extract the superimposed spectra of the SN and its host. For an SN II, we expect Hα to be the brightest feature during the photospheric phase, and in our last epoch (when the spectrum was obtained, see Table 1) AT 2023adsv's flux in F277W (near 3 μm) is ∼14 nJy while the flux in the spectrum is ∼50 nJy at the same wavelength. With nearly three-quarters of the flux contaminated with host light, even if a decomposition were possible, the SN spectrum is likely to have a signal-to-noise ratio of ∼3 pixel^{-1} according to the JWST exposure time calculator.[27] For these reasons, we use the prism spectrum primarily to measure AT 2023adsv's redshift (Figure 2(c)), and the oxygen line ratios to estimate the host's metallicity (see Section 3.1). We report our NIRSpec observation configuration in Table 2.

2.3. Host-galaxy Redshift

AT 2023adsv was discovered in the host galaxy JADES-GS +53.16439-27.83877, and the first step in analyzing AT 2023adsv is to determine its host redshift by identifying prominent emission lines seen in Figure 2. These lines are

---

[22] https://jhat.readthedocs.io

[23] https://github.com/acbecker/hotpants

[24] space-phot.readthedocs.io

[25] https://webbpsf.readthedocs.io

[26] https://spacetelescope.github.io/jdat_notebooks/notebooks/ifu_optimal/ifu_optimal.html

[27] https://jwst-docs.stsci.edu/jwst-exposure-time-calculator-overview

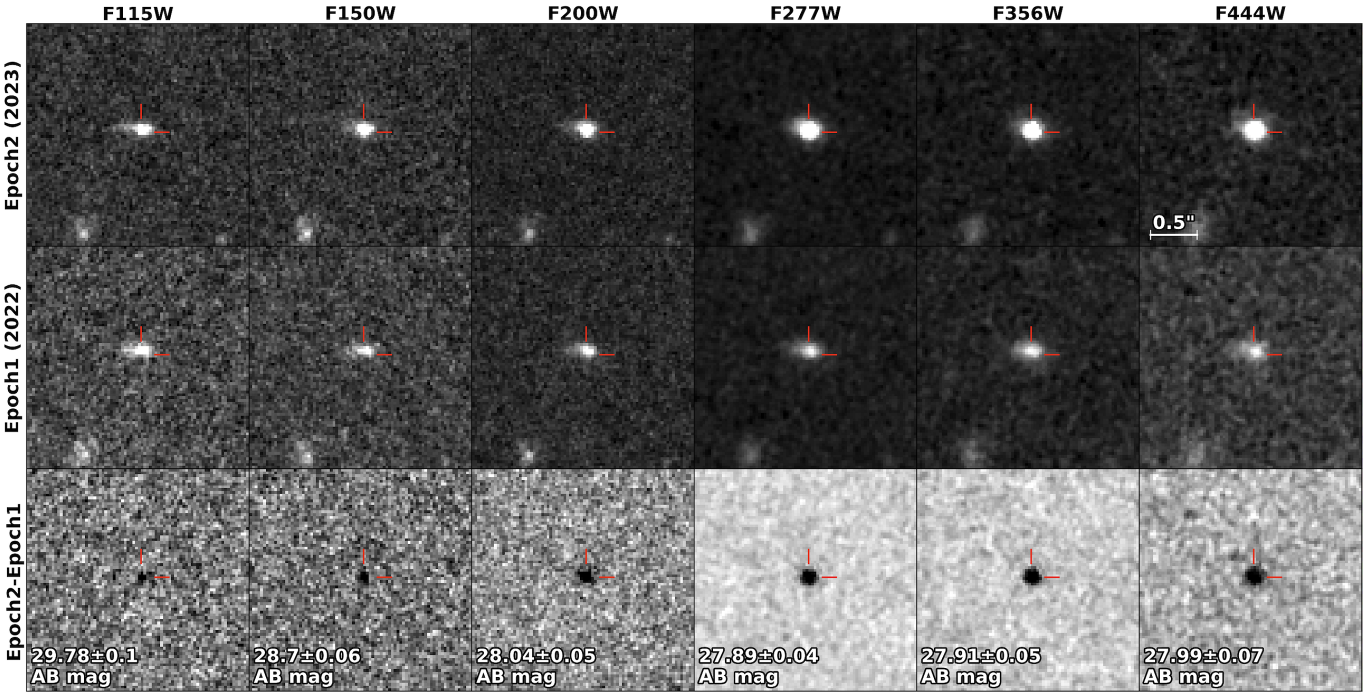

Figure 1. Top and middle rows: JADES Epoch 2 (2023) and Epoch 1 (2022), respectively. AT 2023adsv is present in the 2023 epoch. Bottom row: difference images created by subtracting Epoch 2 from Epoch 1 observations within the same filter. Columns: images in each of six filters reported in Table 1. AT 2023adsv's position is marked with a red indicator. Short-wavelength (F115W, F150W, and F200W) and long-wavelength (F277W, F356W, and F444W) images are drizzled to 0.″03 pixel^{-1} and 0.″06 pixel^{-1}, respectively, and have the same spatial extent.

Table 1
Observations of AT 2023adsv Discussed in Section 2

PID	MJD	Instrument	Filter/ Grating	$m_{\rm AB}$ (mag)	Exp. Time (s)
1180	60215	NIRCam	F115W	29.91 ± 0.09	35,732
1180	60215	NIRCam	F150W	28.75 ± 0.06	23,363
1180	60217	NIRCam	F200W	28.06 ± 0.04	12,368
1180	60215	NIRCam	F277W	27.93 ± 0.04	23,363
1180	60217	NIRCam	F356W	28.00 ± 0.04	12,369
1180	60215	NIRCam	F444W	28.14 ± 0.05	23,363
1180	60276	NIRCam	F115W	>29.6	2512
1180	60276	NIRCam	F150W	>29.7	2512
1180	60276	NIRCam	F200W	28.51 ± 0.13	2512
1180	60276	NIRCam	F277W	28.22 ± 0.12	2512
1180	60276	NIRCam	F356W	28.05 ± 0.10	2512
1180	60276	NIRCam	F444W	28.30 ± 0.21	2512
6541	60310	NIRCam	F150W	>29.5	2512
6541	60310	NIRCam	F200W	29.03 ± 0.14	5025
6541	60310	NIRCam	F277W	28.56 ± 0.17	2512
6541	60310	NIRCam	F356W	28.09 ± 0.12	2512
6541	60310	NIRCam	F444W	28.66 ± 0.28	2512
6541	60310	NIRSpec	prism	⋯	22,175

Note. Columns are JWST Program ID, modified Julian date (MJD), JWST instrument, NIRCam filter, photometry plus final uncertainty for AT 2023adsv, and total exposure time of the Level 3 I2D file rounded to the nearest second. Photometry errors are taken from the PSF fitting posterior, which includes the sky, detector, and Poisson noise. Upper limits are 5σ.

Table 2
AT 2023adsv NIRSpec Observation Details

Instrument	NIRSpec
Mode	MOS
Wavelength range (μm)	0.6–5.3
Slit	Three shutter
(arcsec × arcsec)	(0.46 × 0.2 each)
Grating/filter	prism/CLEAR
$R = \lambda/\Delta\lambda$	~30–300[a]
Readout pattern	NRSIRS2
Groups per integration	19
Integrations per exposure	2
Exposures/nods	3
Total exposure time (s)	22,175

Note.
[a] JWST NIRSpec prism resolving power is a function of wavelength, with $R = 30$ near $\lambda_{\rm obs} \sim 1.1$ μm and $R = 300$ near $\lambda_{\rm obs} \sim 5$ μm; see https://jwst-docs.stsci.edu/jwst-near-infrared-spectrograph/nirspec-instrumentation/nirspec-dispersers-and-filters.

best matched by [O III] and Hα, which have rest-frame wavelengths of ~5008.24 Å and ~6564.61 Å in vacuum, respectively, and provide a robust spectroscopic redshift of $z_{\rm spec} = 3.613 \pm 0.001$. We use this value for all analyses going forward, and present a detailed analysis of these host properties in Section 3.1.

3. Analysis

3.1. Host-galaxy Properties

At a redshift of $z = 3.61$, the host of AT 2023adsv opens a window into the environment of an SN when the Universe was <2 Gyr old. However, because there are no clear SN features in the spectrum of AT 2023adsv, yet we know that SN light must be contaminating the spectrum, any fit of the star formation history (SFH) of JADES-GS+53.16439-27.83877 will be biased by this unaccounted for SN light—with the

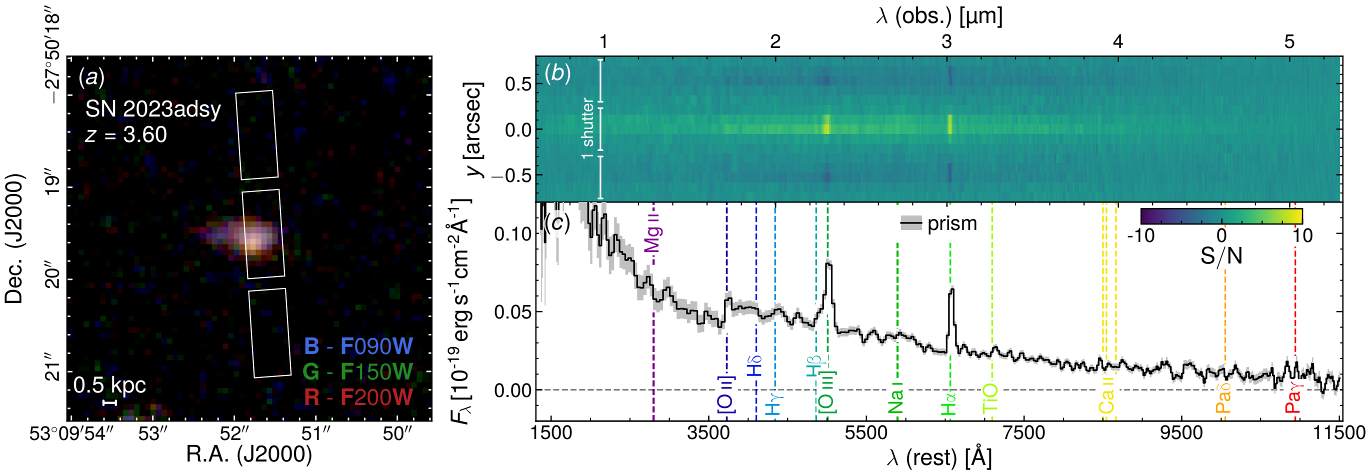

Figure 2. (a) The MSA slit-let position over AT 2023adsv. (b) The 2D NIRSpec prism spectrum of AT 2023adsv and JADES-GS+53.16439-27.83877. We note that the data presented in this 2D spectrum are proportional to units of F_ν. (c) The 1D extracted NIRSpec spectrum for AT 2023adsv transformed into the rest frame in units of F_λ, with host emission lines color coded and labeled. A spectroscopic redshift of $z = 3.613 \pm 0.001$ was measured based on the host's [O III] and Hα lines. No SN features are readily apparent in the resulting 1D spectrum.

added light leading to systematically higher masses, and the SN color altering the inferred stellar properties. To address this, we perform a fit to the pre-SN photometry of the host galaxy to explore the SFH. We fit the JADES photometry of the source measured from the HST Advanced Camera for Surveys in the filters F435W, F606W, F775W, F814W, and F850LP along with JWST/NIRCam in the filters F090W, F115W, F150W, F182M, F200W, F210M, F277W, F335M, F356W, F410M, and F444W. For the fit, we use the tool `Prospector`[28] (B. D. Johnson et al. 2021) and follow the method outlined in J. M. Helton et al. (2026, in preparation). Briefly, within `Prospector` we employ the Flexible Stellar Population Synthesis code (C. Conroy et al. 2009; C. Conroy & J. E. Gunn 2010), and we sampled the posterior distributions of the stellar population properties using the dynamic nested sampling code `dynesty`[29] (J. S. Speagle 2020). We utilize a Chabrier IMF with a lower bound of 0.08 $M_\odot$ and an upper bound of 120 $M_\odot$. Additionally, we assume a delayed-τ star-forming history of the form SFR $\sim t_{\rm age} \times e^{-t_{\rm age}/\tau}$, where $t_{\rm age}$ is the age of the galaxy and τ is the e-folding time. For the fit, we fix the redshift to $z = 3.61$, and allow the stellar- and gas-phase metallicity to vary uniformly between $\log(Z/Z_\odot) = -3.0$–0.0. We plot the `Prospector` fit corresponding to the 50th percentile on the posterior, along with the fit photometry, in Figure 3.

From these fits we estimate a host mass of $\log_{10}(M_*/M_\odot) = 8.41^{+0.12}_{-0.12}$, host age $\log_{10}(t_*/{\rm yr}) = 8.55^{+0.15}_{-0.17}$, and host extinction $A_V = 0.15^{+0.11}_{-0.07}$ mag. These and additional host properties are summarized in Table 3.

Because there are no clear SN features in the spectrum for AT 2023adsv, we rely on the metallicity inferred from the host to estimate the metallicity of the SN. However, while we use `Prospector` to infer host properties like mass, we do not use it to infer the host metallicity because the host spectral energy distribution (SED) modeling can be unreliable due to the strong degeneracy between metallicity and stellar age (A. Dotter et al. 2017). To infer the host metallicity, we instead turn to spectral fitting of the forbidden oxygen lines present in the spectrum (see Figure 2). In the photospheric phase, we do not expect much SN contamination in [O II] and [O III], and use the ratio of [O III] to [O II] (i.e., the O_3O_2 diagnostic from M. Curti et al. 2020) to estimate the metallicity at the position of the SN. We find that $O_3O_2 = 3.0^{+3.2}_{-1.1}$, and assuming a solar metallicity of log(O/H) + 12 =

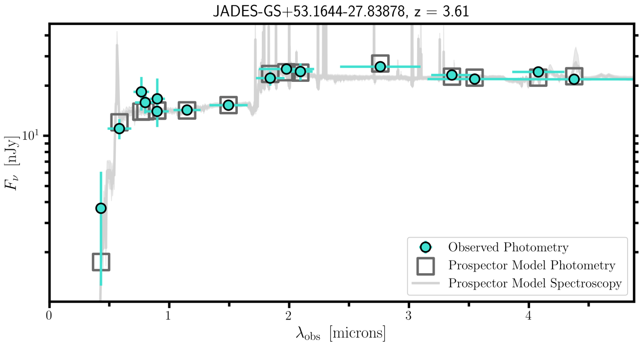

Figure 3. Host template photometry fit using `Prospector`. The blue circles represent the observed JADES pre-SN photometry, and the dark gray shaded line represents the 50th percentile of the final `Prospector` fit to the photometry, with a lighter gray color showing the 16th and 84th percentiles on the fit. The gray boxes are the estimated `Prospector` photometry corresponding to the fit. We provide the derived `Prospector` host-galaxy parameters in Table 3.

Table 3
`Prospector` Derived Host Properties

Parameter	Value
log(age [t_*/yr])	$8.55^{+0.15}_{-0.17}$
log(stellar mass formed [$M_*/M_\odot$])	$8.41^{+0.12}_{-0.12}$
log(SFR/[$M_\odot$yr^{-1}])	$0.31^{+0.08}_{-0.06}$
Gas-phase metallicity [$Z_\odot$][a]	0.3 ± 0.1
log(O/H) + 12[b]	8.1 ± 0.2
A_V [mag]	$0.15^{+0.11}_{-0.07}$

Notes.
[a] We derive a gas-phase metallicity using the oxygen line ratio diagnostic O_3O_2 from M. Curti et al. (2020); see Section 3.1 for a detailed discussion.
[b] We convert between gas-phase metallicity expressed in solar units to units of log(O/H) + 12 following the relation in M. Asplund et al. (2009).

---

[28] https://prospect.readthedocs.io/en/stable/
[29] https://dynesty.readthedocs.io/en/stable/

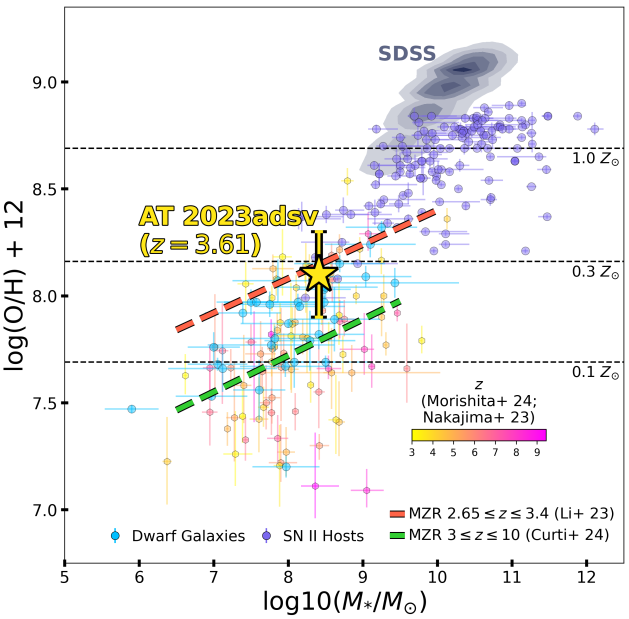

Figure 4. AT 2023adsv's inferred host-galaxy mass and metallicity (gold star) compared to a selection of local galaxies. Gray contours correspond to galaxies selected from SDSS DR8 with $z < 0.7$ (H. Aihara et al. 2011; D. J. Eisenstein et al. 2011), purple points correspond to CCSN hosts (P. L. Kelly & R. P. Kirshner 2012), yellow–pink points correspond to JWST-selected galaxies redshifts at $3 \leqslant z \leqslant 9$ (K. Nakajima et al. 2023; M. Curti et al. 2024; T. Morishita et al. 2024), and blue points correspond to low-metallicity dwarf galaxies from D. A. Berg et al. (2012). The red dashed line corresponds to the MZR for galaxies at $2.65 \leqslant z \leqslant 3.4$ from M. Li et al. (2023); the green dashed line corresponds to the MZR at $3 \leqslant z \leqslant 10$ from M. Curti et al. (2024). Overplotted are horizontal dashed lines, which correspond to the 1.0×, 0.3×, and 0.1 × solar oxygen abundance values derived from M. Asplund et al. (2009).

8.69 (M. Asplund et al. 2009), we find a host oxygen abundance of $\log(\mathrm{O/H}) + 12 = 8.1 \pm 0.2$, or $Z_* \approx 0.3\,Z_\odot$. We note that `Prospector` finds a gas-phase metallicity of $\log(\mathrm{O/H}) + 12 = 7.1 \pm 0.1$, or $Z_* \approx 0.02\,Z_\odot$, ∼an order of magnitude lower. This is a substantial discrepancy, however, we adopt the derivation from the oxygen ratio due to the aforementioned issues when using the integrated fit from `Prospector`. For the remainder of the paper, we adopt a gas-phase metallicity of $\log(\mathrm{O/H}) + 12 = 8.1 \pm 0.2$. This metallicity is notably lower than the mean derived oxygen metallicity found for a collection of SNe II (dominated by SNe IIP) by J. P. Anderson et al. (2010) of $\log(\mathrm{O/H}) + 12 = 8.580 \pm 0.027$.

We place this galaxy in a wider context of SN II hosts in Figure 4. We compare the mass and metallicity of the host of AT 2023adsv with a population of $z < 0.7$ galaxies from the Sloan Digital Sky Survey (SDSS) Data Release (DR8; gray contours; H. Aihara et al. 2011; D. J. Eisenstein et al. 2011), galaxies from JWST with redshifts $3 \leqslant z \leqslant 9$ (yellow–pink points; K. Nakajima et al. 2023; M. Curti et al. 2024; T. Morishita et al. 2024), CCSN hosts (purple points; P. L. Kelly & R. P. Kirshner 2012), and low-metallicity dwarf galaxies (blue points; D. A. Berg et al. 2012). Metallicities for both the SN hosts and SDSS sample were derived following the PP04 O3N2 calibration from M. Pettini & B. E. J. Pagel (2004), while metallicities for both the JWST-selected, high-z sample and dwarf sample were derived using the direct electron-temperature method (A. Campbell et al. 1986). Overplotted are horizontal dashed lines corresponding to the 1.0×, 0.3×, and 0.1 × solar oxygen abundance values converted from M. Asplund et al. (2009), as well as the MZR for galaxies at $2.65 \geqslant z \geqslant 3.4$ from M. Li et al. (2023, red dashed line), and the MZR at $3 \geqslant z \geqslant 10$ from M. Curti et al. (2024, green dashed line). These MZR scalings are supported by recent work with JWST (D. Schaerer et al. 2022; A. J. Taylor et al. 2022; H. Katz et al. 2023; J. E. Rhoads et al. 2023), tracing this relation to even further distances with measurements of two galaxies at $z \approx 8$, and has confirmed that at fixed stellar mass, galaxies are generally less enriched at higher redshift (D. Langeroodi et al. 2023). We find that the metallicity of the host of AT 2023adsv is consistent with the MZR from M. Li et al. (2023) as well as with the lower-metallicity tail of the core-collapse distribution.

3.2. Is AT 2023adsv an Active Galactic Nucleus Flare?

AT 2023adsv was first reported in D25, and in that work nuclear transients corresponding to previously published active galactic nucleus (AGN) catalogs in the GOODS-S field (spanning X-ray to radio, including JWST/MIRI data; J. Lyu et al. 2022; J. Lyu et al. 2024; also see D25 Section 3.3), as well as transient sources that had faded and rebrightened, were removed. Additionally, in the spectrum presented in Figure 2, there is no evidence of broad Mg II emission, primarily associated with Type 1 AGN (L. Č. Popović et al. 2019). Finally, AT 2023adsv is separated from the center of JADES-GS+53.16439-27.83877 by an offset of ∼0$''$.07, which at a redshift of 3.61, corresponds to ∼0.5 kpc—this offset is large enough to be resolved with JWST and generally disfavors an AGN explanation for AT 2023adsv's flux. Taken together with the strength of the light-curve matching in Section 3.3 below, we find that AT 2023adsv is unlikely to be an AGN flare.

3.3. Supernova Light-curve Matching

Following the procedures outlined in Section 5.1 of D25, we fit the measured photometry from Table 1 with a custom extension of `SNCosmo`[30] (K. Barbary et al. 2025) called `STARDUST2`[31] (S. A. Rodney et al. 2014). For a full description of this package's contents see D25. Briefly, `STARDUST2` utilizes SALT3 near-IR SN Ia light-curve models (J. D. R. Pierel et al. 2022) to represent SNe Ia for fitting, as well as over 40 CCSNe spectrophotometric time-series templates. These CCSNe are well-observed, low-z CCSNe and represent a wide range of diversity in each subtype (ranging from SNe II to Type Ib/c SNe), and were originally developed for `SNANA` (R. Kessler et al. 2009). The core functionality of `STARDUST2` is the same as `SNCosmo`, and when referencing these functions below we will simply refer to `STARDUST2`/`SNCosmo` as "`SNCosmo`."

Using `SNCosmo` we fit for SNe Ia, as well as all included CCSN time-series spectral models with rest-frame UV to near-IR (to observer-frame ∼4 μm) wavelength coverage (J. D. R. Pierel et al. 2018, and references therein). In general, `SNCosmo` allows for fitting input photometry by shifting its model SEDs to a desired redshift, and then convolves them with the desired bandpasses to create synthetic photometry of the source. We include Galactic dust based on the maps of E. F. Schlafly & D. P. Finkbeiner (2011) and the reddening law

---

[30] https://sncosmo.readthedocs.io

[31] https://github.com/srodney/starDust2

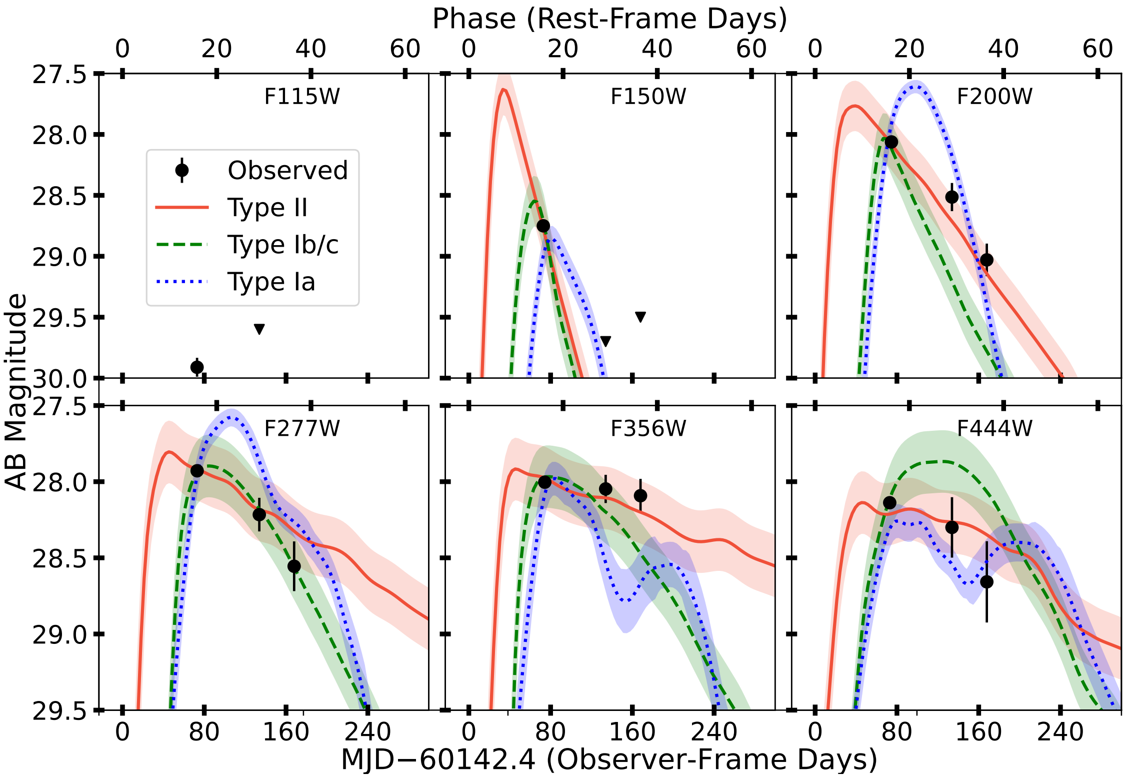

Figure 5. The photometry measured in Section 2.1 is shown as black circles with errors, with (2σ) upper limits denoted by triangles. The best-fit SN II (red solid line), SN Ib/c (green dashed line), and SN Ia (blue dotted line) models are shown for comparison. The time axis is shown relative to MJD 60142.4, chosen as an arbitrary date compatible with each model's varying time of explosion, which is a free parameter of the fitting. The SN II model shown is the SN 2006kv template discussed in Section 3.3. The uncertainties shown are purely statistical.

from E. Fitzpatrick (1999), which corresponds to $E(B-V) = 0.01$ mag with $R_V = 3.1$. We also allow for host-galaxy dust (up to $E(B-V) = 1.5$ mag with $1 < R_V < 5$) of rest-frame, host-galaxy dust in the CCSN light-curve fits and a SALT3 near-IR color parameter range of $-1 < c < 1$.

Figure 5 shows the best-fit models for each SN subtype in all filters plotted relative to MJD 60142.4, chosen as an arbitrary date compatible with each model's varying time of explosion (which is a free parameter of the fitting). The resulting χ^2 per degree of freedom (ν) for each specific model is shown in Table 4. Of the models included in the `SNCosmo` library, the SALT3 near-IR SN Ia and SN Ib/c models, SDSS004012, are heavily disfavored ($\chi^2/\nu = 16.63$ and 6.76, respectively) compared to the best-fitting SN II model, SN 2006kv ($\chi^2/\nu = 1.10$). SN 2006kv is a normal SN IIP discovered at $z = 0.0620$ (C. B. D'Andrea et al. 2010), however, we note that the UV coverage of SN 2006kv's spectral template did not extend to cover AT 2023adsv's F115W detection (at $z = 3.61$, F115W ~ 2500 Å; see Figure 5 and Section 3.4), and therefore is omitted from the fitting. This blue emission could plausibly be due to a more exotic explosion with similarities to an SN II, a possibility that we explore in Section 3.4. While the fit to SN 2006kv is quite good (see Table 4), AT 2023adsv's luminosity required a modeled peak B-band absolute magnitude of -18.3 ± 0.1 mag, ~0.5 mag brighter relative to the real SN 2006kv; while this is still within the range of normal SN IIP absolute magnitudes observed in the local Universe (~3σ above the distribution mean D. Richardson et al. 2014), it is also in agreement with the suggestion from S19 that low-metallicity SNe II could be up to ~0.5 mag brighter than SNe II at high metallicity. We take the results of this light-curve fitting process as conclusive and give AT 2023adsv a classification of SN II as a result.

Table 4
Comparison of the Best-fit Model χ^2 Statistics for Each Supernova Subtype

SN Type	Model/template	χ^2/ν
Ia	SALT3-NIR	16.63
Ib/c	SDSS004012	6.76
II	SN 2006kv	1.10

Note. Columns are SN type, spectral model/template used, and the light-curve fitting χ^2 per degree of freedom (ν) without model uncertainties, as they do not exist for CCSN models.

3.4. Light-curve Modeling

In order to estimate the explosion properties of AT 2023adsv, we compare synthetic light curves with those of AT 2023adsv. For this purpose, we first obtained red supergiant (RSG) SN progenitor models with $0.3\,Z_\odot$ (in agreement with the inferred metallicity measured for its host; see Section 3.1) by using `Modules for Experiments in Stellar Astrophysics (MESA)` version v.23.05.1[32] (B. Paxton et al. 2011, 2013, 2015, 2018, 2019; A. S. Jermyn et al. 2023). We selected a grid of models with ZAMS masses ($M_{\rm ZAMS}$) of 12, 16, and 20 $M_\odot$. The details of the assumptions in the stellar evolution calculations are presented in the

---

[32] In lists available on Zenodo at doi: 10.5281/zenodo.17128107.

Table 5
Progenitor Properties for the Light-curve Computations

M_{ZAMS} ($M_{\odot}$)	M_{fin} ($M_{\odot}$)	$M_{\mathrm{H\text{-}rich}}$ ($M_{\odot}$)	R_{fin} ($R_{\odot}$)
12	11.8	8.6	434
16	14.7	10.0	632
20	15.9	9.5	847
175	163.8	79.4	2499

Note. Columns are ZAMS mass (M_{ZAMS}), final mass at explosion (M_{fin}), hydrogen-rich envelope mass at explosion ($M_{\mathrm{H\text{-}rich}}$), and progenitor radius at explosion (R_{fin}).

accompanying paper (T. J. Moriya et al. 2025). The final progenitor properties are summarized in Table 5.

The RSG progenitor models are then transferred to the 1D multifrequency radiation hydrodynamics code `STELLA` (S. I. Blinnikov et al. 1998, 2006; S. Blinnikov et al. 2000). `STELLA` numerically evaluates the SED evolution of SNe, and thus we can directly estimate light curves in the observer frame (including K-corrections), from the theoretical SED evolution when they appear at $z = 3.6$. We refer to the accompanying paper for the details on the light-curve calculations (T. J. Moriya et al. 2025). Because SNe II are generally found to be embedded within a dense and confined circumstellar medium (CSM; e.g., F. Förster et al. 2018), we also include a version of each of our models with this close-in CSM (deposited up to 10^{15} cm). This approach was taken to account for the amount of UV flux detected in the first epoch (i.e., at $z = 3.6$, F115W and F150W span ∼2500–3250 Å in the rest frame), and the fact that a typical mass-loss rate of $10^{-3}\,M_{\odot}\,\mathrm{yr}^{-1}$ with a wind velocity of $10\,\mathrm{km\,s}^{-1}$, can act as an additional early power source in the light curve (T. Moriya et al. 2011; L. Dessart & D. J. Hillier 2022). The confined CSM masses are $0.07\,M_{\odot}$ ($M_{\mathrm{ZAMS}} = 12\,M_{\odot}$), $0.11\,M_{\odot}$ ($M_{\mathrm{ZAMS}} = 16\,M_{\odot}$), and $0.16\,M_{\odot}$ ($M_{\mathrm{ZAMS}} = 20\,M_{\odot}$).

While the three progenitor models explain the overall properties of AT 2023adsv well, the $M < 20\,M_{\odot}$ models without CSM struggle to reproduce the observed UV flux in the first epoch. Introducing CSM to these less massive models does better at matching the early time UV flux, but are underluminous compared to the first detections in F277W, F356W, and F444W despite boosting their explosion energies to 2.5×10^{51} erg. All models fail to fit the last epoch F200W, F277W, and F444W detections. Despite this, we find that the best overall fit to be the $20\,M_{\odot}$ progenitors (both with and without CSM), and cannot distinguish between them due to not having observations during the time frame of the inferred modeled peak. Therefore, find that the best-fit model to our data is the $0.3\,Z_{\odot}$, $20\,M_{\odot}$ RSG SN progenitor, and present our fit in Figure 6. Notably, we found that higher-mass models with larger explosion energies were required to fit both the luminosity of AT 2023adsv as well as its early blue colors (i.e., the F115W detection).

In general, we find that an explosion energy of $(2\text{–}3) \times 10^{51}$ erg is required to account for the brightness of AT 2023adsv. Comparing to the results of T. J. Moriya et al. (2025), we note that they adopted a progenitor metallicity of $0.1\,Z_{\odot}$ while we use the host-galaxy metallicity of $0.3\,Z_{\odot}$ in this paper. This choice results in slight differences in the estimated progenitor and explosion properties, however, the overall conclusions remain unchanged.

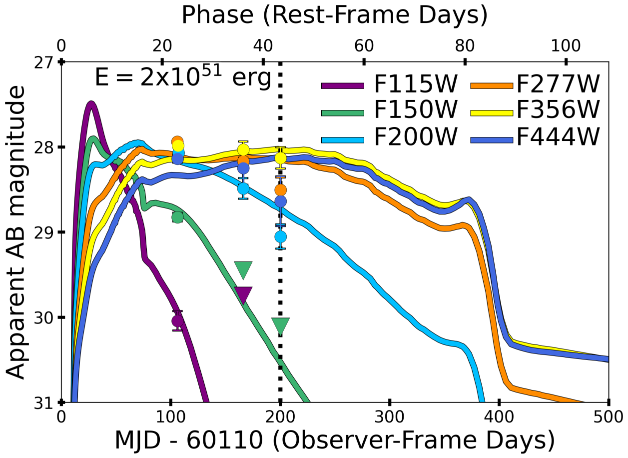

Figure 6. Broadband light curves of the best-fit, $20\,M_{\odot}$, $0.3\,Z_{\odot}$, RSG SN progenitor model in comparison to our photometry. The time axis is shown relative to MJD 60110, chosen as the best fit to our low-metallicity models (and is distinct from the `SNCosmo` explosion time in Figure 5). The vertical dashed line represents the time of the DDT spectrum.

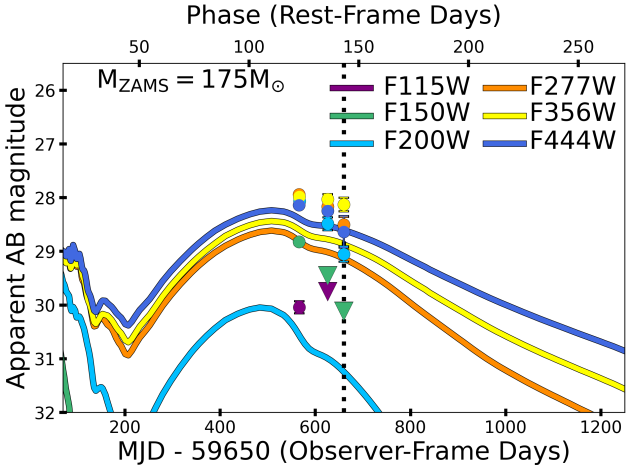

Figure 7. Broadband light curves of the $Z = 0.07\,Z_{\odot}$ metallicity, H-poor PISN model P175 (M. S. Gilmer et al. 2017) in comparison to AT 2023adsv. The time axis is shown relative to MJD 59850, chosen as the best-fit time of explosion for this model. We show that this PISN model, chosen for being one of the few nonzero metallicity PISN models, does not fit the colors or luminosity of AT 2023adsv's photometry.

3.4.1. Pair-instability Explosion

Motivated by exploring an alternative explanation for the measured early blue flux at the redshift of AT 2023adsv, as well as the prediction that pair-instability SNe (PISNe) could form either at relatively high metallicities ($Z_{\odot}/3$, the metallicity of AT 2023adsv's host; N. Langer et al. 2007), or relatively low redshift ($2 < z < 5$; L. Tornatore et al. 2007), we compare PISNe models to our measured photometry. While no explicit $Z_{\odot}/3$ models exist, M. S. Gilmer et al. (2017) have explored H-poor PISN models at $Z = 0.07\,Z_{\odot}$. The best-fit model was that of a $175\,M_{\odot}$ PISN model (P175) with an H-envelope mass of $2.3\,M_{\odot}$ from M. S. Gilmer et al. (2017), shown in Figure 7. Because this particular PISN model is at a metallicity lower than solar, it still retains a fraction of its hydrogen-rich envelope and could spectroscopically appear as an SN II if found early enough in its evolution (<30 days). In general, we find this model a poor fit for AT 2023adsv, both in terms of its luminosity and color, disfavoring a PISN interpretation.

4. Discussion

4.1. AT 2023adsv's Metallicity and Comparison to Low-z Type IIP Supernovae

Owing to the fact that the outermost ejecta of SNe IIP are probed by the photosphere throughout the plateau phase, and the fact that these ejecta are characterized by the molecular clouds from which the pre-SN stars are formed (L. Dessart et al. 2014), definitive assessments of an SN IIP's metallicity are done through detailed spectroscopic studies of the strengths of metal-line absorption during an SN IIP's plateau phase (L. Dessart & D. J. Hillier 2020). In particular, the pEW of Fe II λ5018 has been shown as a proxy for the metallicity of an SN IIP, with larger widths suggesting higher metallicities. This result has been confirmed observationally for the local Universe (J. P. Anderson et al. 2016; F. Taddia et al. 2016; C. P. Gutiérrez et al. 2017, 2018), but relies on spectral coverage during the plateau phase to accurately measure the effect.

In our analysis of AT 2023adsv, we do not have a spectrum with distinct SN features to perform this measurement, but an intriguing study by S19 finds that when comparing the plateau luminosity of a sample of SNe IIP with their host luminosity (in rest-frame r band), spectroscopically confirmed, low-metallicity SNe IIP tend to separate from a "control" sample taken from the literature. Specifically, S19's sample are constructed from "high-contrast" SNe IIP—those with high SN luminosities but with low-luminosity hosts (and therefore low-metallicity hosts), versus a sample of SNe IIP without this property. The central idea is to test the assertion that these high-contrast SNe IIP also have low metallicities as measured in spectra taken during their plateau phase (i.e., because of the inferred low metallicity of low-luminosity hosts via the MZR). S19's result confirms this statistically, and crucially, S19 compares the low-metallicity sample with the control sample photometrically.

Motivated by this, and because AT 2023adsv is well modeled by SN 2006kv, we fit the last observed epoch of AT 2023adsv (F200W, F277W, F356W, and F444W) with a blackbody and find a temperature of ~6200 K—within the range of the recombination temperature of hydrogen, which supports the plateau phase of an SN IIP light curve (5500–7000 K; E. K. Grasberg et al. 1971; S. W. Falk & W. D. Arnett 1977; L. Dessart et al. 2014). Therefore, if we assume that AT 2023adsv is an SN IIP and is within or near the plateau phase in the last observed JWST epoch, we can provisionally compare AT 2023adsv with the sample in S19. We perform K-corrections on both the host and SN photometry, and find that the fitted SN 2006kv model's absolute magnitude (a proxy for AT 2023adsv) at +50 days is -17.5 mag in r band. The resulting comparison is shown in Figure 8.

In this parameter space, AT 2023adsv's high luminosity places its abscissa in the same region as the low-metallicity SNe IIP selected by S19, however, AT 2023adsv's host brightness places its ordinate between the control sample and the low-metallicity sample. The apparent tension of an "overluminous" host for a lower-metallicity SN IIP can be related to the result presented in Figure 4. In the context of an MZR that evolves with redshift (see Section 3.1), we expect that at a fixed stellar mass, the gas-phase metallicity, $\log(\mathrm{O/H}) + 12$, should decrease with increasing redshift (D. Langeroodi et al. 2023; M. Curti et al. 2024). Because we do not correct for this systematic offset between the local data presented in S19 and AT 2023adsv's host at $z = 3.61$, and because S19 infers a metallicity from the the host's luminosity, this trend in MZR has the effect of shifting AT 2023adsv's position in this parameter space closer to the control sample (i.e., those with higher-metallicity hosts).

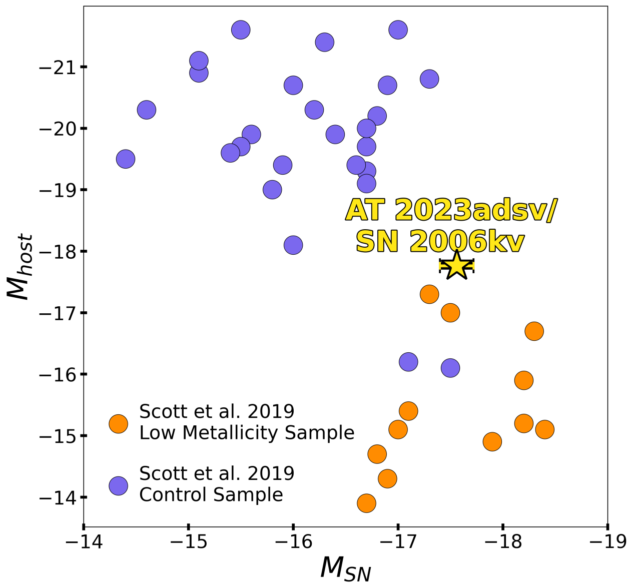

Figure 8. Figure adapted from S19, with a sample of local, low-metallicity-selected SNe IIP (orange points) compared to a "control" sample of local, SNe IIP from the literature (purple points). All photometry is reported in r band, and SN luminosities are taken during the plateau phase. The gold star corresponds to an estimate of AT 2023adsv's plateau absolute magnitude based on the fit to SN 2006kv, were it definitively an SN IIP (see Section 4.1) along with its host luminosity, which occupies a space between the two samples. The errors in the host absolute magnitudes are smaller than the plotted marker.

5. Conclusion

We have presented JWST observations of AT 2023adsv with a spectroscopic redshift of $z = 3.613 \pm 0.001$, discovered by the JADES program. We classify AT 2023adsv using light-curve information as a relatively bright ($M_B = -18.3 \pm 0.1$ mag) SN II. We further model the light curve using the `MESA` code and find a good match to an RSG progenitor star with ZAMS mass 20 $M_\odot$, albeit with a slightly high explosion energy of 2×10^{51} erg. We also compare AT 2023adsv to relatively high-metallicity ($Z = 0.001\,Z_\odot$) PISN models from M. S. Gilmer et al. (2017), however, we find that this comparison is disfavored in both luminosity and color.

While the DDT spectrum of AT 2023adsv confirms its redshift, we could not reliably isolate specific SN features in the spectrum, and we limited our analysis of AT 2023adsv and JADES-GS+53.16439-27.83877 to their photometric properties to prevent bias. Examining the host of AT 2023adsv, JADES-GS+53.16439-27.83877, we find a relatively low-mass ($\log_{10}(M_*/M_\odot) = 8.41^{+0.12}_{-0.12}$), moderately dusty ($A_V = 0.15^{+0.11}_{-0.07}$ mag), low-metallicity ($Z_* = 0.3 \pm 0.1\ Z_\odot$) galaxy. A more careful study of the host environment, and potentially of the SN itself, would be possible with a template spectrum of the host with the same observing parameters in a future JWST cycle—allowing a direct comparison of a spectrum with, and without, contaminating SN light.

AT 2023adsv is one the most distant SNe II with a spectroscopic redshift yet found (see also AT 2023adst, a reported SN II with a host $z = 4.117$; C. DeCoursey et al. 2025), and provides a timely opportunity to study massive SN progenitors at $z > 3$. Intriguingly, AT 2023adsv's inferred metallicity places it in a parameter space between that of low-z, low-metallicity SNe IIP and a control sample of solar-metallicity SNe IIP hosted in massive galaxies. While the best fit to AT 2023adsv was of a massive progenitor with a higher than average explosion energy, testing whether or not there is a trend in SN II properties with increasing redshift and/or decreasing global metallicity—including the possibility of calibrating SNe IIP as metallicity probes of their environments (L. Dessart et al. 2014; J. P. Anderson et al. 2016)—will require larger samples with substantially better spectral coverage. Carefully following up these high-z SNe may lead to novel constraints on the early Universe IMF, as well as metal enrichment and mixing. Upcoming surveys such as the Nancy Grace Roman Space Telescope High Latitude Time Domain Survey (R. Hounsell et al. 2018; B. M. Rose et al. 2021) will likely open a new frontier for this science by finding thousands of distant massive progenitor CCSNe. However, JWST will remain our only resource capable of rest-frame optical–IR imaging and spectroscopy at high z, highlighting the need for building a sample of such observations now and into the future.

Acknowledgments

This paper is based in part on observations with the NASA/ESA/CSA Hubble Space Telescope and James Webb Space Telescope obtained from the Mikulski Archive for Space Telescopes at Space Telescope Science Institute (STScI), which is operated by the Association of Universities for Research in Astronomy, Inc. (AURA), under NASA contract NAS5-03127 for JWST. These observations are associated with programs #1180 and #6541. The JWST data used in this paper can be found in MAST at doi: 10.17909/h522-xx30. We thank the DDT and JWST/HST scheduling teams at STScI for their extraordinary effort in getting the DDT observations used here scheduled quickly. The specific observations analyzed can be accessed via doi: 10.17909/snj9-an10; support was provided to J.D.R.P. and M.E. through program HST-GO-16264. J.D.R.P. is supported by NASA through a Einstein Fellowship grant No. HF2-51541.001 awarded by STScI, which is operated by AURA, for NASA, under contract NAS5-26555. Numerical computations were in part carried out on the PC cluster at the Center for Computational Astrophysics, National Astronomical Observatory of Japan. T.J.M. is supported by the Grants-in-Aid for Scientific Research of the Japan Society for the Promotion of Science (JP24K00682, JP24H01824, JP21H04997, JP24H00002, JP24H00027, and JP24K00668) and by the Australian Research Council (ARC) through the ARC's Discovery Projects funding scheme (project DP240101786). A.J.B. acknowledges funding from the "FirstGalaxies" Advanced Grant from the European Research Council (ERC) under the European Union's Horizon 2020 research and innovation program (grant agreement No. 789056). D.J.E. is supported as a Simons Investigator and by JWST/NIRCam contract to the University of Arizona, NAS5-02015. B.D.J. acknowledges the JWST/NIRCam contract to the University of Arizona, NAS5-02015. R.M. acknowledges support by the Science and Technology Facilities Council (STFC), by the ERC through Advanced grant 695671 "QUENCH," and by the UKRI Frontier Research grant RISEandFALL. R.M. also acknowledges funding from a research professorship from the Royal Society. B.E.R. acknowledges support from the NIRCam Science Team contract to the University of Arizona, NAS5-02015, and JWST Program 3215. S.T. acknowledges support by the Royal Society Research grant G125142. Q.W. is supported by the Sagol Weizmann-MIT Bridge Program. The authors acknowledge use of the lux supercomputer at UC Santa Cruz, funded by NSF MRI grant AST 1828315.

ORCID iDs

D. A. Coulter https://orcid.org/0000-0003-4263-2228
J. D. R. Pierel https://orcid.org/0000-0002-2361-7201
C. DeCoursey https://orcid.org/0000-0002-4781-9078
T. J. Moriya https://orcid.org/0000-0003-1169-1954
M. R. Siebert https://orcid.org/0000-0003-2445-3891
B. A. Joshi https://orcid.org/0000-0002-7593-8584
M. Engesser https://orcid.org/0000-0003-0209-674X
A. Rest https://orcid.org/0000-0002-4410-5387
E. Egami https://orcid.org/0000-0003-1344-9475
M. Shahbandeh https://orcid.org/0000-0002-9301-5302
W. Chen https://orcid.org/0000-0003-1060-0723
O. D. Fox https://orcid.org/0000-0003-2238-1572
L. G. Strolger https://orcid.org/0000-0002-7756-4440
Y. Zenati https://orcid.org/0000-0002-0632-8897
A. J. Bunker https://orcid.org/0000-0002-8651-9879
P. A. Cargile https://orcid.org/0000-0002-1617-8917
M. Curti https://orcid.org/0000-0002-2678-2560
D. J. Eisenstein https://orcid.org/0000-0002-2929-3121
S. Gezari https://orcid.org/0000-0003-3703-5154
S. Gomez https://orcid.org/0000-0001-6395-6702
M. Guolo https://orcid.org/0000-0002-5063-0751
K. Hainline https://orcid.org/0000-0003-4565-8239
J. Jencson https://orcid.org/0000-0001-5754-4007
B. D. Johnson https://orcid.org/0000-0002-9280-7594
M. Karmen https://orcid.org/0000-0003-2495-8670
R. Maiolino https://orcid.org/0000-0002-4985-3819
R. M. Quimby https://orcid.org/0000-0001-9171-5236
P. Rinaldi https://orcid.org/0000-0002-5104-8245
B. Robertson https://orcid.org/0000-0002-4271-0364
S. Tacchella https://orcid.org/0000-0002-8224-4505
F. Sun https://orcid.org/0000-0002-4622-6617
Q. Wang https://orcid.org/0000-0001-5233-6989
T. Wevers https://orcid.org/0000-0002-4043-9400

References

Aihara, H., Allende Prieto, C., An, D., et al. 2011, ApJS, 193, 29
Anderson, J. P., Covarrubias, R. A., James, P. A., Hamuy, M., & Habergham, S. M. 2010, MNRAS, 407, 2660
Anderson, J. P., González-Gaitán, S., Hamuy, M., et al. 2014, ApJ, 786, 67
Anderson, J. P., Gutiérrez, C. P., Dessart, L., et al. 2016, A&A, 589, A110
Anderson, J. P., Dessart, L., Gutiérrez, C. P., et al. 2018, NatAs, 2, 574
Asplund, M., Grevesse, N., Sauval, A. J., & Scott, P. 2009, ARA&A, 47, 481
Barbary, K., Bailey, S., Barentsen, G., et al. 2025, SNCosmo, v2.12.1,
Bazin, G., Palanque-Delabrouille, N., Rich, J., et al. 2009, A&A, 499, 653
Becker, A. 2015, HOTPANTS: High Order Transform of PSF ANd Template Subtraction, Astrophysics Source Code Library, ascl:1504.004
Berg, D. A., Skillman, E. D., Marble, A. R., et al. 2012, ApJ, 754, 98
Blinnikov, S., Lundqvist, P., Bartunov, O., Nomoto, K., & Iwamoto, K. 2000, ApJ, 532, 1132

Blinnikov, S. I., Eastman, R., Bartunov, O. S., Popolitov, V. A., & Woosley, S. E. 1998, ApJ, 496, 454
Blinnikov, S. I., Röpke, F. K., Sorokina, E. I., et al. 2006, A&A, 453, 229
Botticella, M. T., Riello, M., Cappellaro, E., et al. 2008, A&A, 479, 49
Bushouse, H., Eisenhamer, J., Dencheva, N., et al. 2022, JWST Calibration Pipeline, v1.8.2,
Campbell, A., Terlevich, R., & Melnick, J. 1986, MNRAS, 223, 811
Chen, W., Kelly, P. L., Oguri, M., et al. 2022, Natur, 611, 256
Conroy, C., & Gunn, J. E. 2010, ApJ, 712, 833
Conroy, C., Gunn, J. E., & White, M. 2009, ApJ, 699, 486
Cooke, J., Sullivan, M., Gal-Yam, A., et al. 2012, Natur, 491, 228
Curti, M., Mannucci, F., Cresci, G., & Maiolino, R. 2020, MNRAS, 491, 944
Curti, M., Maiolino, R., Curtis-Lake, E., et al. 2024, A&A, 684, A75
Dahlen, T., Strolger, L.-G., Riess, A. G., et al. 2012, ApJ, 757, 70
DeCoursey, C., Egami, E., Pierel, J. D. R., et al. 2025, ApJ, 979, 250
DeCoursey, C., Egami, E., Rieke, M., et al. 2023a, TNSAN, 164, 1
DeCoursey, C., Sun, F., Egami, E., et al. 2023b, TNSAN, 275, 1
Dessart, L., & Hillier, D. J. 2020, A&A, 642, A33
Dessart, L., & Hillier, D. J. 2022, A&A, 660, L9
Dessart, L., Hillier, D. J., Waldman, R., & Livne, E. 2013, MNRAS, 433, 1745
Dessart, L., Gutierrez, C. P., Hamuy, M., et al. 2014, MNRAS, 440, 1856
Dotter, A., Conroy, C., Cargile, P., & Asplund, M. 2017, ApJ, 840, 99
D'Andrea, C. B., Sako, M., Dilday, B., et al. 2010, ApJ, 708, 661
Egami, E., Bonaventura, N., Charlot, S., et al. 2023, JWST, 2, 6541
Eisenstein, D. J., Weinberg, D. H., Agol, E., et al. 2011, AJ, 142, 72
Eisenstein, D. J., Johnson, B. D., Robertson, B., et al. 2025, ApJS, 281, 50
Eisenstein, D. J., Willott, C., Alberts, S., et al. 2026, ApJS, 283, 6
Engesser, M., Brammer, G., Gould, K., et al. 2022a, TNSAN, 145, 1
Engesser, M., Smith, K., Chen, T., et al. 2022b, TNSAN, 155, 1
Falk, S. W., & Arnett, W. D. 1977, ApJS, 33, 515
Ferruit, P., Jakobsen, P., Giardino, G., et al. 2022, A&A, 661, A81
Fitzpatrick, E. 1999, PASP, 111, 63
Förster, F., Moriya, T. J., Maureira, J. C., et al. 2018, NatAs, 2, 808
Gal-Yam, A., Arcavi, I., Ofek, E. O., et al. 2014, Natur, 509, 471
Giavalisco, M., Ferguson, H. C., Koekemoer, A. M., et al. 2004, ApJL, 600, L93
Gilmer, M. S., Kozyreva, A., Hirschi, R., Fröhlich, C., & Yusof, N. 2017, ApJ, 846, 100
Gomez, S., Nicholl, M., Berger, E., et al. 2024, MNRAS, 535, 471
Grasberg, E. K., Imshennik, V. S., & Nadezhin, D. K. 1971, Ap&SS, 10, 3
Graur, O., Poznanski, D., Maoz, D., et al. 2011, MNRAS, 417, 916
Grogin, N. A., Kocevski, D. D., Faber, S. M., et al. 2011, ApJS, 197, 35
Gutiérrez, C. P., Anderson, J. P., Hamuy, M., et al. 2017, ApJ, 850, 89
Gutiérrez, C. P., Anderson, J. P., Sullivan, M., et al. 2018, MNRAS, 479, 3232
Heger, A., Fryer, C. L., Woosley, S. E., Langer, N., & Hartmann, D. H. 2003, ApJ, 591, 288
Horne, K. 1986, PASP, 98, 609
Hounsell, R., Scolnic, D., Foley, R. J., et al. 2018, ApJ, 867, 23
Jermyn, A. S., Bauer, E. B., Schwab, J., et al. 2023, ApJS, 265, 15
Johnson, B. D., Leja, J., Conroy, C., & Speagle, J. S. 2021, ApJS, 254, 22
Katz, H., Saxena, A., Cameron, A. J., et al. 2023, MNRAS, 518, 592
Kelly, P. L., & Kirshner, R. P. 2012, ApJ, 759, 107
Kessler, R., Bernstein, J. P., Cinabro, D., et al. 2009, PASP, 121, 1028
Koekemoer, A. M., Faber, S. M., Ferguson, H. C., et al. 2011, ApJS, 197, 36
Lahén, N., Naab, T., & Szécsi, D. 2024, MNRAS, 530, 645
Langer, N., Norman, C. A., de Koter, A., et al. 2007, A&A, 475, L19
Langeroodi, D., Hjorth, J., Chen, W., et al. 2023, ApJ, 957, 39
Larson, R. B. 1998, MNRAS, 301, 569
Li, M., Cai, Z., Bian, F., et al. 2023, ApJL, 955, L18
Lyu, J., Alberts, S., Rieke, G. H., & Rujopakarn, W. 2022, ApJ, 941, 191
Lyu, J., Alberts, S., Rieke, G. H., et al. 2024, ApJ, 966, 229
Melinder, J., Dahlen, T., Mencía Trinchant, L., et al. 2012, A&A, 545, A96
Mokiem, M. R., de Koter, A., Vink, J. S., et al. 2007, A&A, 473, 603
Morishita, T., Stiavelli, M., Grillo, C., et al. 2024, ApJ, 971, 43
Moriya, T., Tominaga, N., Blinnikov, S. I., Baklanov, P. V., & Sorokina, E. I. 2011, MNRAS, 415, 199
Moriya, T. J., Coulter, D. A., DeCoursey, C., et al. 2025, PASJ, 77, 851
Nakajima, K., Ouchi, M., Isobe, Y., et al. 2023, ApJS, 269, 33
Paxton, B., Bildsten, L., Dotter, A., et al. 2011, ApJS, 192, 3
Paxton, B., Cantiello, M., Arras, P., et al. 2013, ApJS, 208, 4
Paxton, B., Marchant, P., Schwab, J., et al. 2015, ApJS, 220, 15
Paxton, B., Schwab, J., Bauer, E. B., et al. 2018, ApJS, 234, 34
Paxton, B., Smolec, R., Schwab, J., et al. 2019, ApJS, 243, 10
Pettini, M., & Pagel, B. E. J. 2004, MNRAS, 348, L59
Pierel, J. D. R., Coulter, D. A., Siebert, M. R., et al. 2025, ApJ, 981, L9
Pierel, J. D. R., Engesser, M., Coulter, D. A., et al. 2024a, ApJL, 971, L32
Pierel, J. D. R., Frye, B. L., Pascale, M., et al. 2024b, ApJ, 967, 50
Pierel, J. D. R., Jones, D. O., Kenworthy, W. D., et al. 2022, ApJ, 939, 11
Pierel, J. D. R., Newman, A. B., Dhawan, S., et al. 2024c, ApJL, 967, L37
Pierel, J. D. R., Rodney, S., Avelino, A., et al. 2018, PASP, 130, 114504
Popov, D. V. 1993, ApJ, 414, 712
Popović, L. Č., Kovačević-Dojčinović, J., & Marčeta-Mandić, S. 2019, MNRAS, 484, 3180
Postman, M., Coe, D., Benítez, N., et al. 2012, ApJS, 199, 25
Rest, A., Pierel, J., Correnti, M., et al. 2023, arminrest/jhat: The JWST HST Alignment Tool (JHAT), v2,
Rest, A., Stubbs, C., Becker, A. C., et al. 2005, ApJ, 634, 1103
Rhoads, J. E., Wold, I. G. B., Harish, S., et al. 2023, ApJL, 942, L14
Richardson, D., Jenkins, R. L. I., Wright, J., & Maddox, L. 2014, AJ, 147, 118
Rodney, S. A., Riess, A. G., Strolger, L.-G., et al. 2014, AJ, 148, 13
Rose, B. M., Baltay, C., Hounsell, R., et al. 2021, arXiv, arXiv:2111.03081
Sanders, N. E., Soderberg, A. M., Gezari, S., et al. 2015, ApJ, 799, 208
Schaerer, D., Marques-Chaves, R., Barrufet, L., et al. 2022, A&A, 665, L4
Schlafly, E. F., & Finkbeiner, D. P. 2011, ApJ, 737, 103
Scott, S., Nicholl, M., Blanchard, P., Gomez, S., & Berger, E. 2019, ApJL, 870, L16
Siebert, M. R., Decoursey, C., Coulter, D. A., et al. 2024, ApJL, 972, L13
Smartt, S. J. 2009, ARA&A, 47, 63
Smith, N. 2014, ARA&A, 52, 487
Speagle, J. S. 2020, MNRAS, 493, 3132
Strolger, L.-G., Dahlen, T., & Riess, A. G. 2010, ApJ, 713, 32
Strolger, L.-G., Dahlen, T., Rodney, S. A., et al. 2015, ApJ, 813, 93
Strolger, L.-G., Rodney, S. A., Pacifici, C., Narayan, G., & Graur, O. 2020, ApJ, 890, 140
Taddia, F., Moquist, P., Sollerman, J., et al. 2016, A&A, 587, L7
Taylor, A. J., Barger, A. J., & Cowie, L. L. 2022, ApJL, 939, L3
Tornatore, L., Ferrara, A., & Schneider, R. 2007, MNRAS, 382, 945
Tucker, M. A., Hinkle, J., Angus, C. R., et al. 2024, ApJ, 976, 178
Valenti, S., Howell, D. A., Stritzinger, M. D., et al. 2016, MNRAS, 459, 3939
Vink, J. S., de Koter, A., & Lamers, H. J. G. L. M. 2001, A&A, 369, 574
Woosley, S. E., Heger, A., & Weaver, T. A. 2002, RvMP, 74, 1015
Wu, S., & Fuller, J. 2021, ApJ, 906, 3
Ziegler, J. J., Edwards, T. D. P., Suliga, A. M., et al. 2022, MNRAS, 517, 2471